

Comparing Low-Mach and Fully-Compressible CFD Solvers for Phenomenological Modeling of Nanosecond Pulsed Plasma Discharges with and without Turbulence

Taaresh Sanjeev Taneja* and Suo Yang[†]

Department of Mechanical Engineering, University of Minnesota – Twin Cities, Minneapolis, MN 55455, USA

This work aims at comparing the accuracy and overall performance of a low-Mach CFD solver and a fully-compressible CFD solver for direct numerical simulation (DNS) of nonequilibrium plasma assisted ignition (PAI) using a phenomenological model described in Castela et al. [1]. The phenomenological model describes the impact of nanosecond pulsed plasma discharges by introducing source terms in the reacting flow equations, instead of solving the detailed plasma kinetics at every time step of the discharge. Ultra-fast gas heating and dissociation of O_2 are attributed to the electronic excitation of N_2 and the subsequent quenching to ground state. This process is highly exothermic, and is responsible for dissociation of O₂ to form O radicals; both of which promote faster ignition. Another relatively slower process of gas heating associated with vibrational-to-translational relaxation is also accounted for, by solving an additional vibrational energy transport equation. A fully-compressible CFD solver for high Mach (M>0.2) reacting flows, developed by extending the default rhoCentralFoam solver in OpenFOAM, is used to perform DNS of PAI in a 2D domain representing a cross section of a pin-to-pin plasma discharge configuration. The same case is also simulated using a low-Mach, pressure-based CFD solver, built by extending the default reactingFoam solver. The lack of flow or wave dominated transport after the plasma-induced weak shock wave leaves the domain causes inaccurate computation of all the transport variables, with a rather small time step dictated by the CFL condition, with the fully-compressible solver. These issues are not encountered in the low-Mach solver. Finally, the low-Mach solver is used to perform DNS of PAI in lean, premixed, isotropic turbulent mixtures of CH₄-air at two different Reynolds numbers of 44 and 395. Local convection of the radicals and vibrational energy from the discharge domain, and straining of the high temperature reaction zones resulted in slower ignition of the case with the higher Re. A cascade effect of temperature reduction in the more turbulent case also resulted in a five - six times smaller value of the vibrational to translational gas heating source term, which further inhibited ignition. Two pulses were sufficient for ignition of the Re = 44 case, whereas three pulses were required for the Re = 395 case; consistent with the results of Ref. [1].

I. Nomenclature

u_i	=	<i>i</i> th velocity component
e	=	total internal energy per unit mass
e_{vib}	=	vibrational energy per unit mas
h_s	=	sensible enthalpy per unit mass
e_s	=	sensible internal energy per unit mass
H	=	total non-chemical enthalpy per unit mass
\boldsymbol{E}	=	total non-chemical energy per unit mass
p	=	gas pressure
T	=	gas temperature
t	=	time
ho	=	gas density

^{*}Ph.D. Candidate, Student Member AIAA.

[†]Richard & Barbara Nelson Assistant Professor, suo-yang@umn.edu (Corresponding Author), Senior Member AIAA.

 $\tau_{ij} = \text{viscous stress tensor}$ $\sigma_{ij} = \text{total stress tensor}$

 $D_{N_2} = diffusion coefficient of N_2$ $e_{sk} = sensible energy of species k$ $\Delta h_{f,k}^o = formation enthalpy of species k$ $Y_k = mass fraction of species k$

 $V_{k,i} = i^{th}$ component of the mixture-averaged diffusion velocity of species k

 $\dot{\omega}_k^c$ = net molar production rate of species k due to combustion

 Q_{reac} = heat release rate due to combustion reactions

 C_v = specific heat at constant volume

 R_u = universal gas constant σ_{pulse} = input energy density

r = radial coordinate in the discharge zone

 τ_{pulse} = plasma pulse duration

 η = fraction of total deposited power used for dissociating O_2

 α = fraction of total deposited power towards vibrational energy production

 e_{vib}^{eq} = equilibrium vibrational energy per unit mass τ_{VT} = time-scale of vibrational-to-translational relaxation

 Y_{O_2} = instantaneous mass fraction of oxygen $Y_{O_2}^f$ = mass fraction of oxygen in fresh mixture R_{λ} = Taylor microscale Reynolds number Re_L = Integral length scale Reynolds number

II. Introduction

TANOSECOND non-equilibrium plasma assisted combustion (PAC) has gained popularity due to its relatively lower Ninout power requirements, fast gas heating, the possibility of leveraging non-equilibrium plasma chemistry at low temperatures [2] and the ease of non-equilibrium plasma igniter integration within practical combustors to promote faster ignition, reduce emissions as well as ensure flame stability at harsh operating conditions (e.g., in ultra-lean combustion, and in scramjets). At atmospheric pressure, different regimes of the plasma have been observed depending on the voltage difference and the gap distance between the electrodes, pulsing frequencies and the ambient gas temperature [3]. Different models focus on different aspects of PAC modeling. 0D models, as described in Refs. [4, 5], etc. are often developed to investigate detailed PAC kinetics in a constant pressure / volume reactor. 1D models, as described in Refs. [6, 7], provide detailed electric field distribution which further helps in accurately modeling plasma kinetic source terms and ambipolar diffusion effects. However, these models are limited to analyzing diffused, homogeneous discharges between parallel plates or any such 0D/1D configurations which are typically observed only at low pressures. Detailed 2D models which solve for the plasma and combustion kinetics in addition to flow dynamics, as described by Pancheshnyi and Starikovskiy [8] and Sharma et al. [9], can successfully predict streamer formation and subsequent conduction channel formation to form a glow / spark discharge, but these models are very computationally expensive. Hence, these are only used for ignition of simple fuels such as H₂, and are limited to quiescent / laminar flows. Tholin and Bourdon [10] described a detailed 2D model which couples sub-models for the streamer phase, nanosecond spark phase and afterglow phase, which can potentially reduce the computational overhead by making certain assumptions about the time-scales of pressure relaxation which can allow neglecting the impact of pressure or kinetics on the flow during the pulse. A relatively simple and computationally feasible 2D / 3D model to simulate PAC in turbulent flows was proposed by Castela et al. [1], which is a phenomenological model that accounts for the effects of the plasma using source terms specific to the discharge assumptions, but obviates solving for detailed plasma kinetics and discharge dynamics altogether. This makes the 2D/3D simulation of turbulent PAC with multiple pulses computationally feasible. The current work aims to implement this model using OpenFOAM with two different computational fluid dynamics (CFD) solvers - a pressure-based, low-Mach solver and a fully-compressible, high Mach solver, which are described in the next section. The performance of both solvers are compared based on two cases of plasma discharges in quiescent air. Section III.A consists of the exact equations solved, and a description of the numerical schemes of both the solvers. The procedure to obtain real and divergence-free isotropic turbulent velocity field in 2D is also described in section III.B. The results for different cases - a single pulse validation case, verification cases of multiple pulsed plasma discharges in quiescent air and lean premixed CH₄-air mixtures, and PAI of isotropic turbulent CH₄-air mixtures is provided in

III. Numerical Methodology

A. Equations, Model Details and Numerical Schemes

The phenomenological model proposed in Ref. [1] has been implemented here based on two different CFD solvers within the OpenFOAM [11] platform. The major difference being that the fully compressible solver (named rhoCentralPlasmaFoam - RCPF) uses only the equation of state (EOS), Eq. (6), to compute the pressure from the energy / enthalpy and density, whereas the "low-Mach" solver (or pressure-based solver) (named CanteraPlasmaFoam -CPF) solves the pressure-Poisson equation, Eq. (7), with an EOS based corrector for density. The Poisson equation acts as an explicit corrector for velocity, which ensures that it satisfies continuity. Post density correction, energy / enthalpy and temperature are also predicted with the updated pressure, velocity and density values from the first stage of predictor-corrector equations. A second stage of correction is used to again correct for the velocity, pressure and density based on the momentum equations, pressure Poisson (from continuity) equation and the EOS using the predicted values of energy / enthalpy. The detailed procedure is explained in Ref.[12], which is also used in the default reactingFoam solver in OpenFOAM, with the addition of the mass fraction equations to the predictor-corrector iterations. Two versions of the fully-compressible solver, namely rhoCentralEPlasmaFoam (RCEPF) and rhoCentralHPlasmaFoam (RCHPF), which solve for the total non-chemical energy and total non-chemical enthalpy, respectively, are used and compared in this work. The corresponding two versions of the low-Mach solver, CanteraEPlasmaFoam (CEPF) and CanteraHPlasmaFoam (CHPF) have no difference in terms of accuracy and performance. Thus, they are both referred to as CanteraPlasmaFoam (CPF), henceforth. CanteraPlasmaFoam is based on the default reactingFoam solver, and thus, uses the compressible PIMPLE algorithm (i.e., a coupled PISO-SIMPLE algorithm) to update the density, velocity, pressure and energy fields as described above. Second order interpolation schemes are used for spatial discretization (gradient, divergence and laplacian terms), and the first order Euler implicit scheme is used for time integration. The fully compressible, rhoCentralPlasmaFoam solver uses the second order central-upwind scheme [13] to discretize the convective and diffusive flux terms in the conservative equations Eqs. (1), (4), (5) and (8), and the first order Euler implicit scheme for time integration.

These solvers are developed in-house by coupling (default) reacting Foam and rho Central Foam with Cantera [14] (an open-source suite of tools for problems involving chemical kinetics, thermodynamics, and transport processes). Transport equations for the solution of the species mass fractions, along with additional transport and source terms associated with species are added to the energy / enthalpy equation to extend the non-reacting fully-compressible solver, (default) rho Central Foam, to a reacting version. Both these solvers use mixture-averaged transport and detailed finite-rate chemistry. The details of these base solvers, without plasma modeling, have been provided in Refs. [15, 16]. Moreover, the numerical schemes and the implementation details of the default non-reacting fully-compressible solver, rho Central Foam, are laid out in Ref. [17].

The plasma discharge power density is modeled using Eq. (12), which is based on the assumption that the power density between two pin electrodes stays confined to a cylindrical discharge zone [18], and remains constant with time during the entire pulse. This source term is switched on periodically for a few nanoseconds and then is turned off for a long period of time (10 - 100's of μ s) before the next pulse. The constants a and b in Eq. (12) can be obtained by ensuring that the integration of the energy density over the volume results in the total deposited energy (700 μ J in this case). In this work, a and b are chosen to be 6.915×10^{-8} m² and 2.5 respectively, as suggested in Ref. [19]. The detailed derivation of the source terms representing the plasma discharge is provided in Ref. [1]. In Eqs. (5), (2) and (4), $\dot{\omega}_k^p$ is the net production rate of the k^{th} plasma species, \dot{E}^p is the total power density which is then assumed to be divided into ultra-fast gas heating, \dot{E}_{heat}^p , ultra-fast dissociation of O_2 , \dot{E}_{chem}^p , and ultra-fast increase of vibrational power density, \dot{E}_{vib}^p . \dot{R}_{VT}^p represents the slower gas heating associated with the vibrational-to-translational relaxation, which is calculated using the Landau-Teller harmonic oscillator model as is done in Ref. [1]. The time-scale for this relaxation is obtained using an empirical formulation proposed in Millikan and White [20]. The equations solved by both solvers are listed below.

$$\frac{\partial(\rho u_j)}{\partial t} + \frac{\partial(\rho u_i u_j)}{\partial x_i} = -\frac{\partial p}{\partial x_j} + \frac{\tau_{ij}}{\partial x_i}$$
 (1)

$$\frac{\partial(\rho e)}{\partial t} + \frac{\partial(\rho u_i e)}{\partial x_i} = -\frac{\partial q_i}{\partial x_i} + \frac{\partial(\sigma_{ij} u_i)}{\partial x_i} + \dot{E}^p_{chem} + \dot{E}^p_{heat} + \dot{R}^p_{VT} \tag{2}$$

$$e = \frac{1}{2}u_i u_i + \sum_{k=1}^{N_{sp}} (e_{s,k} + \Delta h_{f,k}^o) Y_k$$
 (3)

$$\frac{\partial (\rho e_{vib})}{\partial t} + \frac{\partial (\rho u_i e_{vib})}{\partial x_i} = -\frac{\partial}{\partial x_j} \left(\rho D \frac{\partial e_{vib}}{\partial x_i} \right) + \dot{E}^p_{vib} - \dot{R}^p_{VT} \tag{4}$$

$$\frac{\partial(\rho Y_k)}{\partial t} + \frac{\partial(\rho u_i Y_k)}{\partial x_i} = -\frac{\partial}{\partial x_i} \left(\rho V_{k,i} Y_k \right) + W_k \dot{\omega}_k^c + W_k \dot{\omega}_k^p \tag{5}$$

$$P = \frac{\rho R_u}{C_v} \left(e - \frac{1}{2} u_i u_i \right) \tag{6}$$

$$\frac{\partial}{\partial x_i} \left(\frac{\partial p}{\partial x_i} \right) = -\frac{\partial}{\partial x_i} \left(\frac{\partial (\rho u_i u_j)}{\partial x_j} \right) \tag{7}$$

$$\frac{\partial(\rho H)}{\partial t} + \frac{\partial(\rho u_i H)}{\partial x_i} = -\frac{\partial q_i}{\partial x_i} + \frac{\partial(\tau_{ij} u_i)}{\partial x_i} + \frac{\partial p}{\partial t} - \frac{\partial}{\partial x_i} \left(\rho \sum_{k=1}^{N_{sp}} h_{s,k} Y_k V_{k,i} \right) + \dot{Q}_{reac} + \dot{E}_{heat}^p + \dot{R}_{VT}^p \tag{8}$$

$$\frac{\partial(\rho E)}{\partial t} + \frac{\partial(\rho u_i E)}{\partial x_i} = -\frac{\partial q_i}{\partial x_i} + \frac{\partial(\sigma_{ij} u_i)}{\partial x_i} - \frac{\partial}{\partial x_i} \left(\rho \sum_{k=1}^{N_{sp}} h_{s,k} Y_k V_{k,i}\right) + \dot{Q}_{reac} + \dot{E}_{heat}^p + \dot{R}_{VT}^p$$
(9)

$$H = h_s + \frac{1}{2}u_i u_i \tag{10}$$

$$E = e_s + \frac{1}{2}u_i u_i \tag{11}$$

Since only O_2 is assumed to undergo dissociation during the discharge pulse in this model, $\dot{\omega}_k^p$ reduces to ω_O^p and $\omega_{O_2}^p$. The plasma source terms are defined as follows:

$$\dot{E}^{p} = \frac{\sigma_{pulse}}{\tau_{pulse}} erfc \left(\frac{r^{2}}{a}\right)^{b} \tag{12}$$

$$\dot{\omega}_{O}^{p} = \eta \frac{Y_{O_{2}}}{Y_{O_{2}}^{f}} \frac{\dot{E}^{p}}{e_{O}}$$

$$\dot{\omega}_{O_{2}}^{p} = -\frac{W_{O}}{W_{O_{2}}} \dot{\omega}_{O}^{p}$$
(13)

$$\dot{E}_{chem}^{p} = \frac{\eta Y_{O_2}}{Y_{O_2}^f} \left(1 - \frac{W_O e_{O_2}}{W_{O_2} e_O} \right) \dot{E}^p \tag{14}$$

$$\dot{E}_{heat}^{p} = \alpha \dot{E}^{p} - \dot{E}_{chem}^{p} \tag{15}$$

$$\dot{E}_{vib}^{p} = (1 - \alpha)\dot{E}^{p} \tag{16}$$

$$\dot{R}_{VT}^{p} = \frac{\rho(e_{vib} - e_{vib}^{eq}(T))}{\tau_{VT}}$$
 (17)

$$e_{vib}^{eq}(T) = \frac{\frac{R_u}{W_{N_2}}\Theta_1}{e^{\Theta_1/T} - 1}$$
 (18)

$$\tau_{VT} = \left(\frac{1}{\tau_{VT}^{O}} + \frac{1}{\tau_{VT}^{O_2}} + \frac{1}{\tau_{VT}^{N_2}}\right)^{-1} \tag{19}$$

The values for η and α are set to 0.35 and 0.55, respectively, by calculating the average energy required for the electronic excitation of N_2 and its subsequent quenching and formation of O radicals. This process also liberates heat, which is estimated to be equal to the deficit of the energy balance for the dissociation reaction. Experimental evidence [18] is further used to justify the choice of the parameter values. The next section shows the effect of N_2 dissociation on ignition by assuming N_2 = 0.35 (with dissociation) and N_3 = 0 (without dissociation).

All simulations are performed in a 2D square domain representing the cross section of a reactor with pin-to-pin plasma discharges. Wave-transmissive, non-reflecting boundary conditions are used for all the solution variables at the edges of this domain. These boundary conditions (BC's) are preferred over zero-gradient BC's to avoid numerical reflection of the acoustic wave, which propagates radially outwards within a few microseconds after the plasma pulse ends. The advection equation, Eq. (20), is solved for all the variables (denoted as ϕ) at the boundary. The wave velocity in this case is given by Eq. (21), where \vec{U}_n is the flow velocity normal to the boundary and c is the speed of sound.

$$\frac{\partial \phi}{\partial t} + \vec{W}_n \cdot \nabla_n \phi = 0 \tag{20}$$

$$\vec{W}_n = \vec{U}_n + c\vec{n} \tag{21}$$

The default reactingFoam solver in OpenFOAM only offers unity Lewis number transport modeling, and thus Cantera is coupled to this solver in order to use the more accurate mixture-averaged transport model [15]. The transonic option is used with this solver to use the PIMPLE algorithm that allows relatively precise calculation for unsteady flows even at relatively higher Mach numbers (up to M 2), which are observed when the heated plasma kernel expands after the pulse is turned off, as is shown in Refs. [1, 10]. A 512×512 uniform mesh is used for all the simulations. The time step size during the pulses is fixed at 1 ns, and the maximum time step size used during the gaps between pulses is limited to 50 ns. Thus, the CFL condition was used to dynamically calculate the time step sizes during the gaps between plasma pulses.

B. 2D homogeneous isotropic turbulence (HIT) initial conditions

A pseudo-spectral code is developed for initializing the homogeneous isotropic turbulent (HIT) velocity field in a 2D domain. An approach similar to Rogallo's procedure [21] for 3D HIT is used in this work. The two conditions for ensuring the 2D divergence-free and real values of the velocity vector in physical space remain the same as the original 3D case, and can be given by

$$\vec{k} \cdot \vec{u} = 0$$

$$\hat{u}_i(\vec{k}) = \hat{u}_i^*(-\vec{k})$$
(22)

Here, \vec{u} and \vec{k} stand for the transformed 2D velocity vector in the wave number space and the 2D wave number vector, respectively. Following Rogallo's procedure, \vec{u} can be expressed as

$$\vec{\hat{u}} = \alpha(k)[k_2\hat{e}_1 - k_1\hat{e}_2] \tag{23}$$

$$\alpha = \frac{1}{k} \sqrt{\frac{E(k)}{2\pi k}} e^{i\theta} \tag{24}$$

In Eq. (24), θ is a random real number between 0 and 2π and E(k) is the assumed Passot-Pouquet spectrum [22] in 2D, given by

$$E(k) = \frac{32}{3} \sqrt{\frac{2}{\pi}} \frac{u'^2}{k_0} \left(\frac{k}{k_0}\right)^4 exp\left(-2\left(\frac{k}{k_0}\right)^2\right)$$
 (25)

where u' is the non-dimensional RMS turbulent velocity and k_0 is the non-dimensional wave number corresponding to the length scale possessing the maximum energy.

while
$$((p - p_{old}) / p > \epsilon)$$
:
$$\frac{\partial(\rho H)}{\partial t}|^* + \frac{\partial(\rho u_i H)}{\partial x_i}|^n = \frac{\partial p}{\partial t}|^n + \dot{E}_{heat}^p|^n$$
update p using EOS and then update $\frac{\partial p}{\partial t}$

$$\frac{\partial(\rho H)}{\partial t}|^{n+1} = \frac{\partial(\rho H)}{\partial t}|^* - \frac{\partial q_i}{\partial x_i}|^{n+1} + \frac{\partial(\tau_{ij}u_i)}{\partial x_i}|^{n+1} - \frac{\partial}{\partial x_i}\left(\rho\sum_{k=1}^{N_{sp}}h_{s,k}Y_kV_{k,i}\right)|^{n+1} + \dot{Q}_{reac}|^{n+1} + \dot{R}_{VT}^p|^n + \dot{E}_{heat}^p|^n$$

Fig. 1 Inner loop to compute $\frac{\partial p}{\partial t}$.

IV. Results and Discussion

A. Validation with experimental data

Plasma discharges in pre-heated air at 1500 K were modeled using RCEPF, RCHPF and CPF solvers, and the results are compared in Fig. 2. Initial number density of 3×10^{17} particles per cm³ was set for the O radicals in this case, consistent with Ref. [1]. In the fully-compressible solvers, the convective terms in the momentum, mass fraction, and energy / enthalpy equations are treated explicitly, whereas the diffusion terms are added as implicit correction terms to the matrix of coefficients at the current time step. This strategy is extended from the original non-reacting solver, rhoCentralFoam, to this version to prevent extremely small time step sizes limited by the time-scales of the diffusive terms. The net reaction source terms in the mass fraction equations, $W_k \dot{\omega}_k^c$ and the heat release terms in the energy / enthalpy equations, \dot{Q}_{reac} , are computed using CVODE [23], which is an implicit ODE solver. Thus, splitting errors are potential sources of issues with these solvers. Moreover, the enthalpy equation in RCHPF has an additional $\partial p/\partial t$ term which is added to the RHS of Eq. (8) and is iterated over, within a single time-step, to achieve a converged estimate before advancing the solution of the total non-chemical enthalpy equation. This is done to obtain pressure from the calculated density and enthalpy such that they obey the equation of state at each time step, before evaluating its temporal derivative. The equation solved during each sub-iteration excludes the implicit diffusion terms. This is shown in Eq. (26).

$$\frac{\partial(\rho H)}{\partial t}|^* + \frac{\partial(\rho u_i H)}{\partial x_i}|^n = \frac{\partial p}{\partial t}|^n + \dot{E}_{heat}^p|^n$$
(26)

The plasma source terms, \dot{E}_{heat}^p and \dot{R}_{VT}^p , are added explicitly to avoid reduction of the diagonal dominance of the

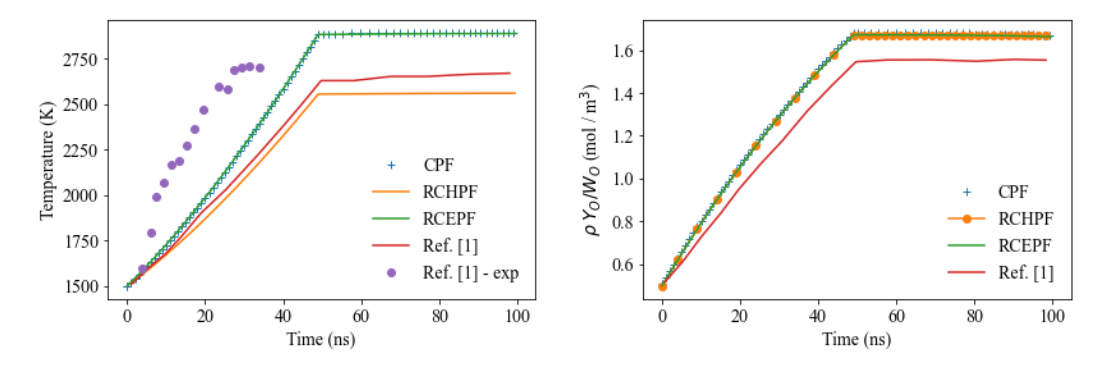


Fig. 2 Single Pulse Validation: Maximum Temperature and O radical concentration using CanteraPlasmaFoam and rhoCentralPlasmaFoam compared with [1].

system of equations as these are positive "source" terms on the RHS. It was observed that if \dot{E}^p_{heat} was added after the updated $\partial p/\partial t$ loop, with the implicit diffusive terms, the max temperature reduced to almost 2550 K at the end of the pulse. However, keeping it in Eq. (26) resulted in a max temperature of around 2850 K, which is within 2% error as compared to the other solvers. The final update equation of ρH , with \dot{E}^p_{heat} added to this step is shown in Eq. (27). Moreover, since \dot{E}^p_{heat} (fast gas heating mode) is almost 3 - 4 orders of magnitude larger than \dot{R}^p_{VT} (slow gas heating mode) during the 50 ns pulse, the addition of \dot{R}^p_{VT} either in Eq. (26) or in Eq. (27) does not make an appreciable

difference. And since most reactions for this case are not exothermic, the same explanation holds for the addition of the heat release term \dot{Q}_{reac} . Since this discrepancy associated with the $\partial p/\partial t$ loop is not present in the total non-chemical energy equation, all the further simulations done using the fully-compressible solver use the RCEPF version, instead of the RCHPF version.

The maximum temperature and the O radical concentration plots in Fig. 2 show that CPF and RCEPF match very closely, but they both over-predict the solutions as compared to the data provided in Ref. [1]. The reason for this over-prediction will be investigated in the future.

$$\frac{\partial(\rho H)}{\partial t}|^{n+1} = \frac{\partial(\rho H)}{\partial t}|^* - \frac{\partial q_i}{\partial x_i}|^{n+1} + \frac{\partial(\tau_{ij}u_i)}{\partial x_i}|^{n+1} - \frac{\partial}{\partial x_i}\left(\rho\sum_{k=1}^{N_{sp}}h_{s,k}Y_kV_{k,i}\right)|^{n+1} + \dot{Q}_{reac}|^{n+1} + \dot{R}_{VT}^p|^n + \dot{E}_{heat}^p|^n$$
(27)

B. Nanosecond repetitively pulsed plasma (NRP) discharges in air

Next, a simulation with multiple discharge pulses in quiescent air at an initial temperature of 300 K was performed using the CPF and RCEPF solvers. The comparison of the temperature at the domain center for the first five pulses has been shown in Fig. 3(a). Excellent agreement was achieved for both the cases; $\eta = 0.35$ - with O_2 dissociation and $\eta = 0$ - without O_2 dissociation, with respect to Ref. [1] using the low-Mach solver (CPF). A weak shock wave (with a shock Mach number of ~ 1.09) was observed immediately after the end of the 50 ns discharge pulse, which propagates radially outwards and later transitions to an acoustic wave (Fig. 4 (a) and (b)). As shown in Fig. 3(b), agreement in terms of the maximum temperature was observed for both the CPF and RCEPF solvers until the acoustic wave is present in the domain. The acoustic wave induced flow reaches a maximum Mach number of ~ 0.24 at the end of the pulse, which then reduces to almost ~ 0 as the heat kernel spreads outwards. However, major differences were observed after $\sim 6\mu s$, when there is negligible transport due to flow or waves in the domain, after the acoustic wave exits the domain.

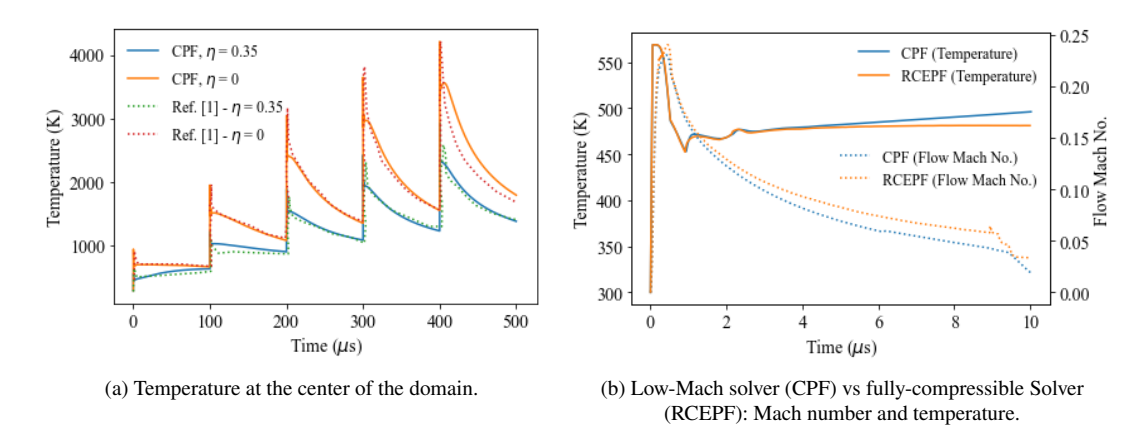


Fig. 3 Comparison of temperature with [1] using both the fully-compressible solver (RCEPF) and low-Mach solver (CPF)

Moreover, the fully-compressible solver, RCEPF, showed asymmetric distribution of temperature and all other variables (Fig. 4 (d)), with respect to the angular (θ) direction. While central schemes such as the ones developed in Kurganov et al. [13], [24] and used in Greenshields et al. [17] do not involve any characteristic decomposition of the fluxes, and offer a framework that is independent of the eigenstructure of the problem, local speeds of propagation are used, nonetheless, to compute the weights of the outward and inward direction fluxes at a given face. Extremely low Mach number flows could cause numerical errors in the computation of these fluxes which are based on the local speeds of propagation. While this is a speculation, the exact cause of such asymmetry with RCEPF will be investigated in the future. Nevertheless, this issue can possibly be attributed to the central-upwind scheme based on a comparison test done with another fully compressible solver, PeleC [25], which uses the piecewise parabolic method for spatial discretization, an approximate Riemann solver for flux computation. The results with the latter (not shown here) do not have such asymmetry. Solvers that solve the elliptic pressure Poisson equation using PIMPLE method, used in CPF, convert the solution of the system of equations to solution of individual equations by iterative predictor-corrector schemes. Hence,

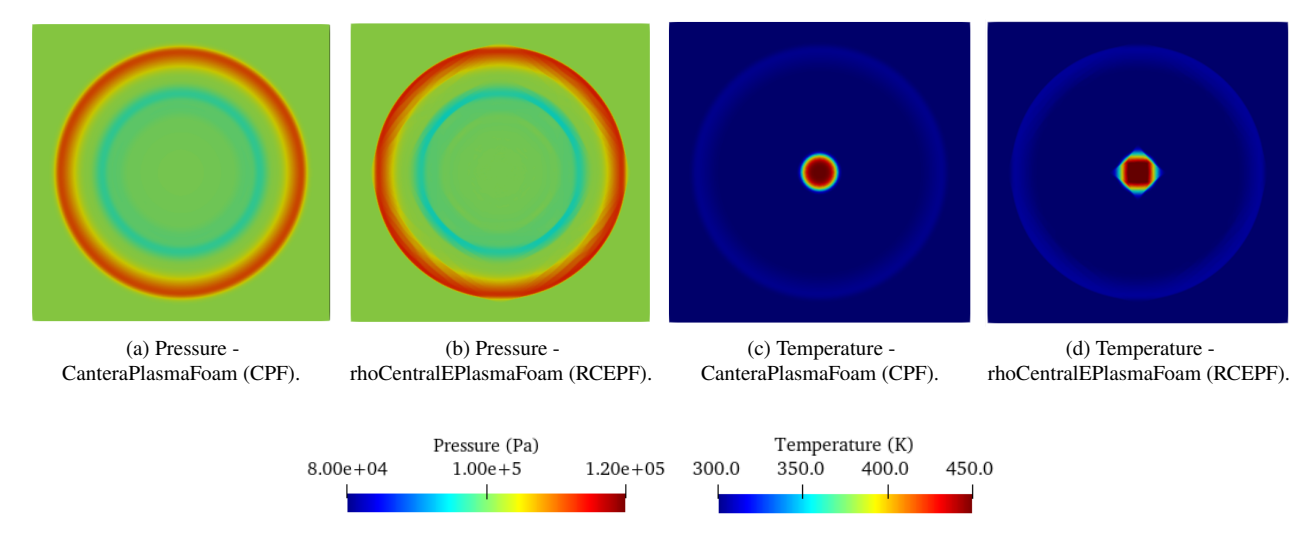


Fig. 4 Pressure wave and temperature kernel at $t = 5 \mu s$: comparison between the low-Mach solver (CPF) and fully-compressible solver (RCEPF).

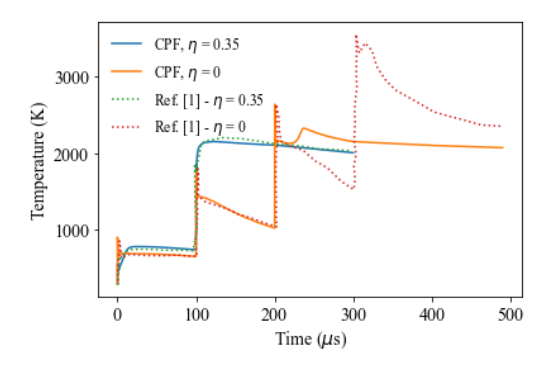
such an issue does not arise with CPF. A closer observation of Fig. 4(b) shows the propagating pressure wave is smeared. This could be a result of the low order of accuracy (second order) and high artificial viscosity associated with the central upwind scheme used in RCEPF solver. However, the exact cause is yet to be determined. Numerical diffusion associated with this scheme is also evident in the 1D shock tube case presented with the default non-reacting rhoCentralFoam solver in Ref. [17].

Furthermore, as is discussed in Refs. [26, 27], using fully-compressible solvers for low speed flows, without any special numerical treatment (e.g., preconditioning [28, 29]), can result in both poor accuracy and computational inefficiency. Both these effects were observed, as the RCEPF solver diverged from the expected solution during the gaps between the plasma pulses and also required a time step lesser than 1 ns even after the pulses, which made the simulations at least two orders of magnitude slower, as compared to the low-Mach, CPF, solver.

C. NRP discharges in CH₄-air mixtures – quiescent and homogeneous isotropic (HIT) turbulent conditions

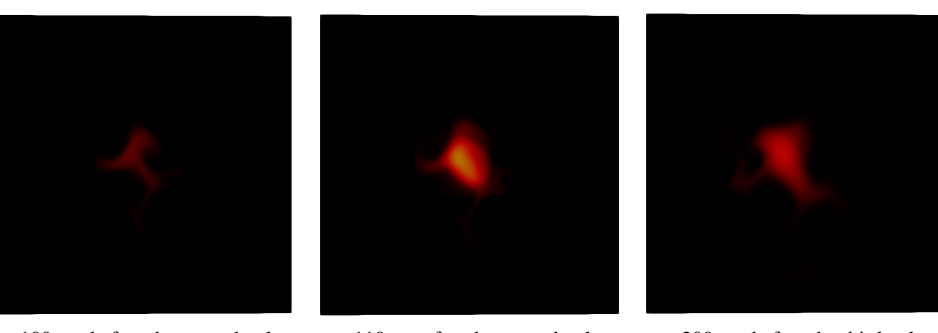
Ignition simulations using NRP discharges were performed in quiescent and isotropic turbulent, lean premixed mixtures ($\phi = 0.8$) of CH₄-air using the GRI 3.0 mechanism [30]. The initial temperature and pressure were set to 300 K and 1 atm, respectively, for all the cases. Figure 5 shows the verification plot of maximum temperature for both $\eta = 0.35$ and $\eta = 0$ cases at quiescent initial conditions. Two pulses were sufficient to ignite the mixture which was assisted by O₂ dissociation to produce O radicals, same as Ref. [1]. However, differences were observed for the case without O₂ dissociation. While 4 pulses were required for ignition in Ref. [1], only 3 pulses were sufficient for ignition with the CPF solver developed in the current research. A rapid rise in OH and O radical concentrations was observed from 0.21 to 0.23 ms, which indicates ignition. Given the good agreement of results until 0.21 ms, a possible explanation for the early ignition in the current work could be the difference in combustion chemistry mechanism. Castela et al. [1] used a 29 species mechanism which was not available, whereas the current work uses the GRI 3.0 mechanism. The differences in the reaction rate coefficients or thermodynamic/transport properties, at high temperatures, might have led to this difference, which will be investigated.

Ignition of the same mixture in homogeneous isotropic (HIT) turbulent conditions with integral length scale based Re = 44 and Re = 395 was simulated to evaluate the effect of turbulence on the convection of radicals from the discharge zone, straining of the hot-spots formed after each pulse and the transport of vibrational energy. The corresponding Taylor-scale Reynolds numbers were approximately 25 and 75, thereby preserving the proportionality $R_{\lambda} = c \cdot Re_{L}^{0.5}$. The large-scale turbulent fluctuating velocities were set as 2 m/s and 6 m/s, respectively, for each of the cases and the non-dimensional wave number corresponding to the most energetic scale was chosen as 8.0. This was based on the length scale of 0.625 mm for the most energetic scale, and the domain size of 5 mm, given in Ref. [1]. The 2D Passot-Pouquet spectrum was used to determine the initial turbulent velocity field computed using Eqs. (23)-(25). The



Maximum temperature comparison for CH₄ ignition in quiescent medium with Ref. [1]

impact of turbulence on ignition kernel development for the Re = 395 case was much more pronounced as compared to the Re = 44 case. The former needed three pulses whereas the latter only needed two pulses to ignite. Figure 6 shows the development of the ignition kernel at the different instants of the simulation. At $t = 100 \mu s$, just before the second plasma pulse, the relatively fast moving eddies in the Re = 395 case (Fig.7 (a)) as compared to the ones in the Re = 44 case (Fig. 7 (b)) strain the high temperature zone. Moreover, the radicals O (Fig. 8 (a)), OH, CO, which are known to be chiefly responsible for heat release, also get convected away from the center of the domain, where the plasma discharge is irradiated. Both turbulent transport and molecular diffusion seem to a have a greater effect for the high Re case, as is expected, with the former being much more dominant. This also shows up in the relatively distributed nature of the chemical heat release rate for the Re = 395 case (Fig. 8 (b)), as compared to the Re = 44 case (Fig. 8 (f)). A similar observation is also made for the vibrational energy (Fig. 8 (c) and (g)). An obvious consequence of the reduced vibrational energy in the discharge zone explains the reduction in the vibrational-to-translational relaxation source term, R_{VT} . A cascade effect of lower temperature and lower concentration of O radicals at the center of the domain also reduces R_{VT} . This is because the time scale of collision and resultant quenching of the vibrational excited states of N_2 is inversely proportional to the concentrations of O, O_2 and N_2 . While the concentrations of O_2 and O_3 remain almost similar in the discharge zone for both the cases, the O radicals are more concentrated around the discharge periphery in the Re = 44 case (Fig.8 (e)). Hence, the overall time scale of relaxation could be slightly greater in the high turbulence case, which could also explain the relatively lower value of R_{VT} in the discharge zone (Fig. 8 (d)) as compared to Fig. 8 (h) (refer Eq. (17)). Closer comparison of Fig. 7 (a), (e) and (b), (f) suggests that the velocity field is only affected in the discharge zone in both the cases, after the 50 ns pulse is irradiated. Thus, there is almost negligible interaction of the weak shock wave (turned acoustic wave within a few μ s of emanating radially) with turbulence. Greater shock-turbulence interaction is certainly expected for a stronger shock wave. Thus, the ignition characteristics are solely determined by the conditions prevailing before the second pulse, which are clearly more favorable for the Re = 44 case, as compared to the Re = 395 case. Eventually, after about 40 μ s post the third plasma pulse, ignition kernel development commenced for the Re = 395 case. Favorable conditions for ignition were observed simply because of the extra ultra-fast gas heating, O radical generation and VT relaxation due to the third pulse. This can be seen clearly in Fig. 9.



 $t = 100 \mu s$, before the second pulse. $t = 110 \mu s$, after the second pulse.

 $t = 200 \mu s$, before the third pulse.

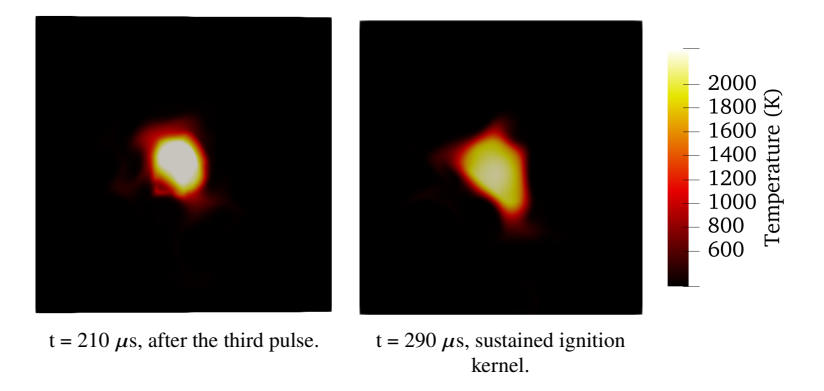


Fig. 6 Ignition after 3 pulses - 2D HIT (DNS), Re = 395.

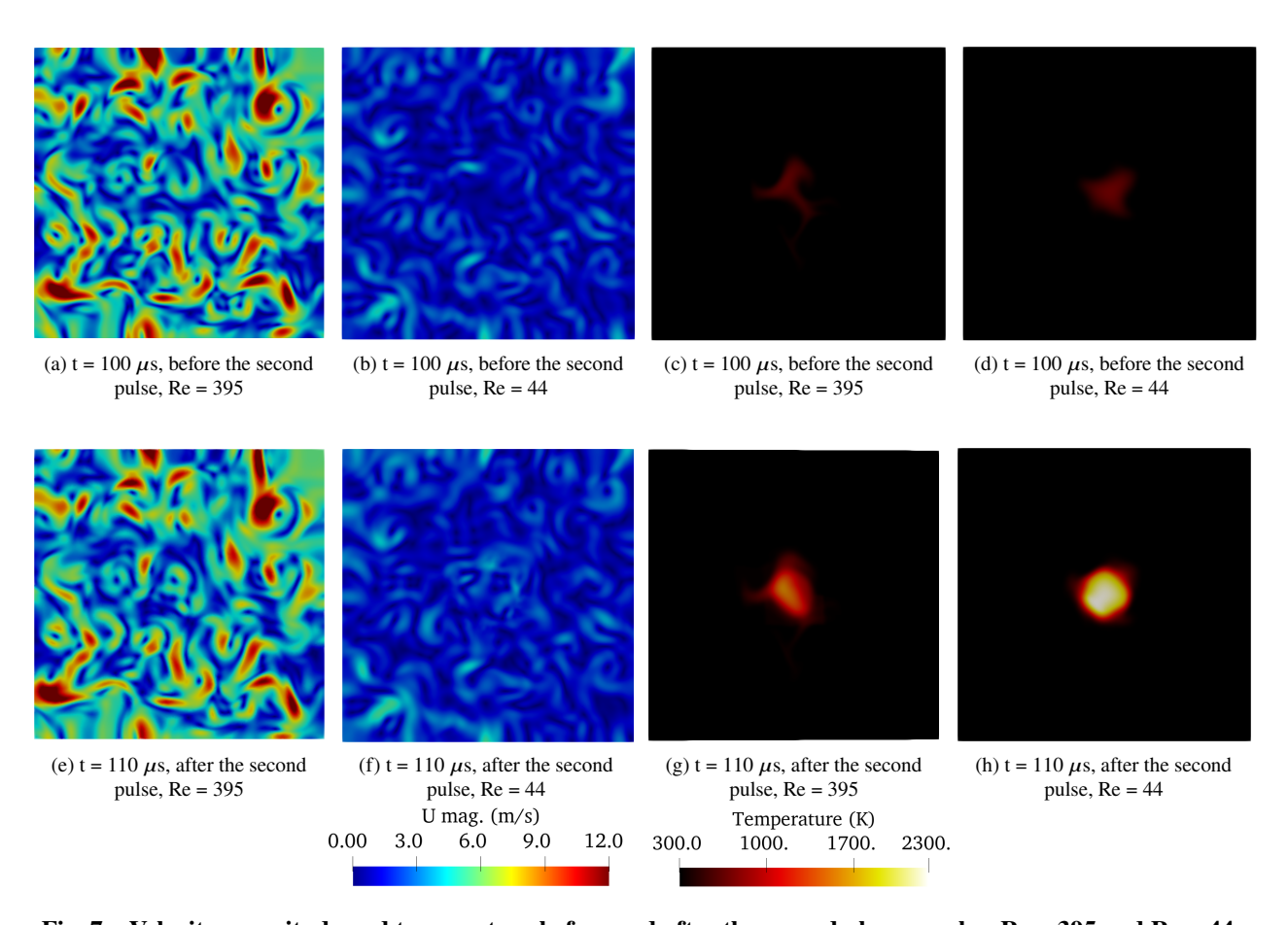


Fig. 7 Velocity magnitude and temperature before and after the second plasma pulse, Re = 395 and Re = 44

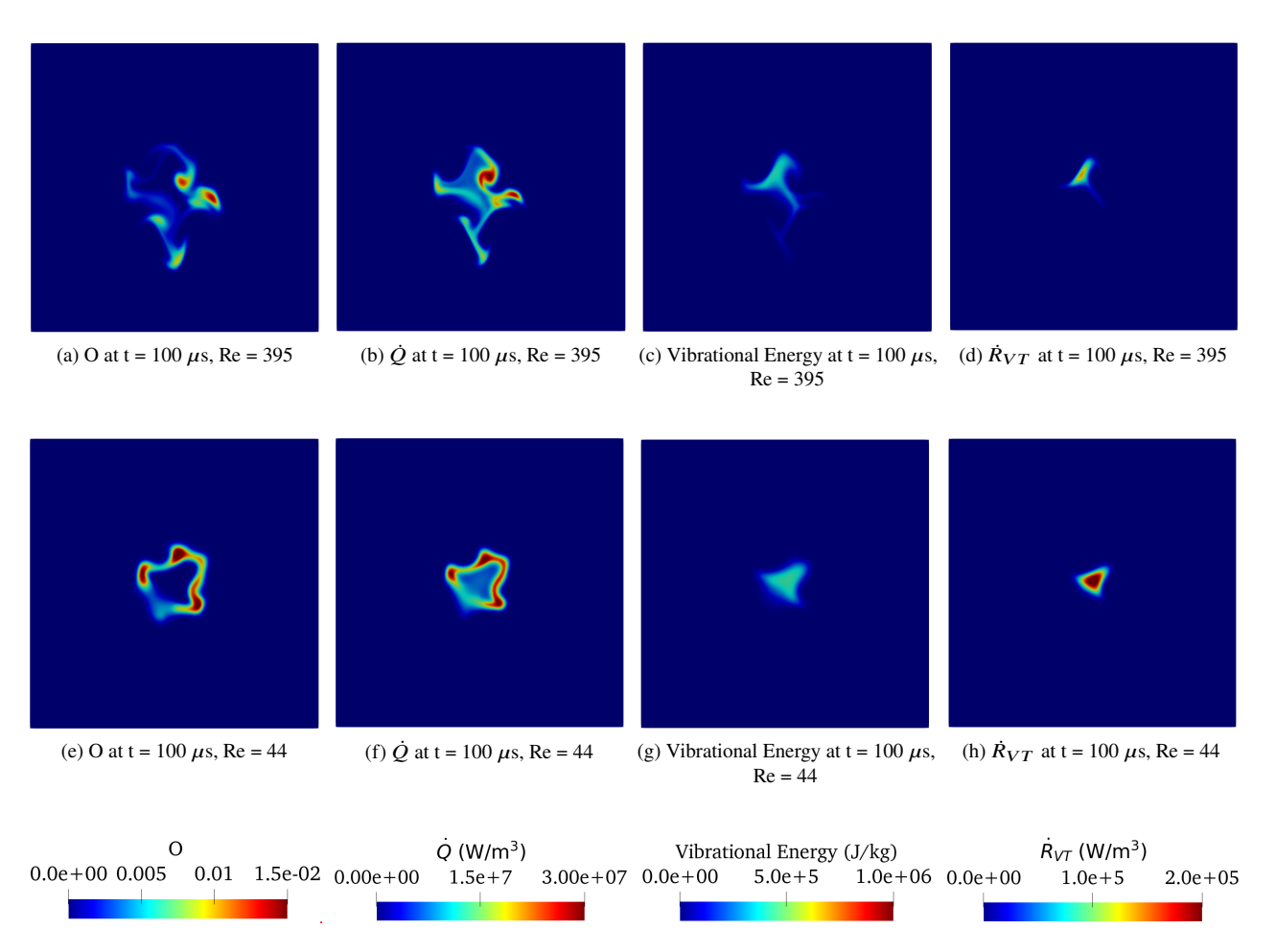


Fig. 8 Comparison of factors responsible for ignition failure (Re = 395) and ignition success (Re = 44) right before the second pulse

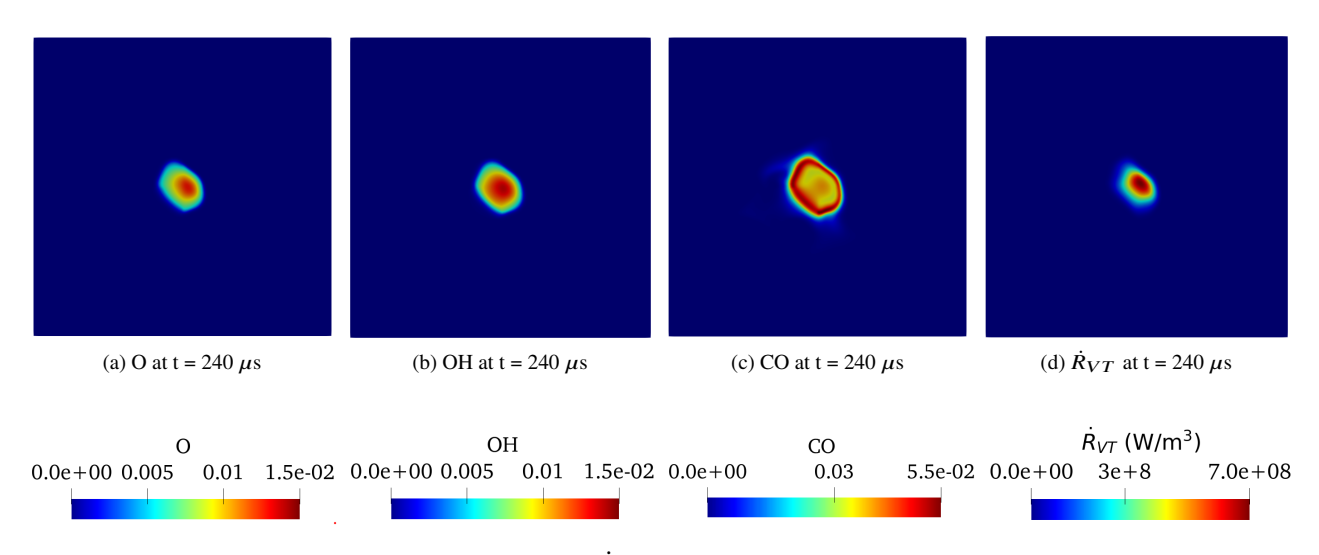


Fig. 9 Mass fractions of important radicals and \dot{R}_{VT} during ignition kernel development at t = 240 μ s, Re = 395 case

V. Conclusion

CanteraPlasmaFoam (CPF), a pressure-based low Mach solver, and rhoCentralEPlasmaFoam (RCEPF), a fully-compressible high Mach solver, were developed by extending the base reacting flow solvers with the phenomenological model to simulate pin-to-pin plasma discharges in a 2D square domain, described in Ref. [1]. Accuracy and efficiency issues were encountered by RCEPF, especially in cases which lacked transport due to flow / waves. Both solvers were in good agreement with each other for the single pulse validation case, where a weak shock wave developed after the end of the discharge pulse and propagated radially outwards from the center of the domain. However, for cases with multiple discharges, the RCEPF solver was at least two orders of magnitude slower as compared to CPF, due to the stringent CFL number requirement posed by the extremely low Mach number flow in the domain. Results from CPF, on the other hand agreed quite well with the data provided in Ref. [1] for both discharges in air and premixed CH₄-air mixtures.

The importance of the input plasma energy contribution towards dissociation of O_2 to form O radicals was clearly witnessed while simulating NRP discharge based ignition of lean premixed CH_4 -air mixture in a quiescent medium. Two pulses were needed for the ignition of the mixture with higher O radical concentration due to the plasma discharge, as compared to the three pulses required by the case with lesser reactivity due to lower O radical production. Finally, the impact of turbulence on PAI was also investigated and the results were found to be consistent with Ref. [1]. Local convection of radicals and straining of the high temperature zones, for the case with higher turbulence, was noted to be the primary cause of ignition failure. The convection of the high vibrational energy away from the regions of high temperature and rich radicals also exacerbated the chances of ignition, as the vibrational to translational relaxation source term was reduced. The relative effect of these factors will be quantified in the future, and would be investigated for different flow and discharge configurations.

Acknowledgments

S. Yang acknowledges the grant support from NSF CBET 2002635. T.S. Taneja acknowledges the support from the UMII MnDRIVE Graduate Assistantship Award. The authors acknowledge Dr. Dezhi Zhou for his contributions towards developing the base solvers which are extended in this work. T.S. Taneja acknowledges the useful discussions with Dr. Maria Castela, Mr. Surya Narayan and Mr. Navneeth Srinivasan.

References

- [1] Castela, M., Fiorina, B., Coussement, A., Gicquel, O., Darabiha, N., and Laux, C. O., "Modelling the impact of non-equilibrium discharges on reactive mixtures for simulations of plasma-assisted ignition in turbulent flows," *Combustion and flame*, Vol. 166, 2016, pp. 133–147.
- [2] Ju, Y., Lefkowitz, J. K., Reuter, C. B., Won, S. H., Yang, X., Yang, S., Sun, W., Jiang, Z., and Chen, Q., "Plasma assisted low temperature combustion," *Plasma Chemistry and Plasma Processing*, Vol. 36, No. 1, 2016, pp. 85–105.
- [3] Pai, D. Z., Lacoste, D. A., and Laux, C. O., "Transitions between corona, glow, and spark regimes of nanosecond repetitively pulsed discharges in air at atmospheric pressure," *Journal of Applied Physics*, Vol. 107, No. 9, 2010, p. 093303.
- [4] Lefkowitz, J. K., Guo, P., Rousso, A., and Ju, Y., "Species and temperature measurements of methane oxidation in a nanosecond repetitively pulsed discharge," *Philosophical Transactions of the Royal Society A: Mathematical, Physical and Engineering Sciences*, Vol. 373, No. 2048, 2015, p. 20140333.
- [5] Taneja, T. S., and Yang, S., "Numerical Modeling of Plasma Assisted Pyrolysis and Combustion of Ammonia," *AIAA Scitech* 2021 Forum, 2021, p. 1972.
- [6] Yang, S., Nagaraja, S., Sun, W., and Yang, V., "Multiscale modeling and general theory of non-equilibrium plasma-assisted ignition and combustion," *Journal of Physics D: Applied Physics*, Vol. 50, No. 43, 2017, p. 433001.
- [7] Yang, S., Gao, X., Yang, V., Sun, W., Nagaraja, S., Lefkowitz, J. K., and Ju, Y., "Nanosecond pulsed plasma activated C2H4/O2/Ar mixtures in a flow reactor," *Journal of Propulsion and Power*, Vol. 32, No. 5, 2016, pp. 1240–1252.
- [8] Pancheshnyi, S., and Starikovskii, A. Y., "Two-dimensional numerical modelling of the cathode-directed streamer development in a long gap at high voltage," *Journal of Physics D: Applied Physics*, Vol. 36, No. 21, 2003, p. 2683.
- [9] Sharma, A., Subramaniam, V., Solmaz, E., and Raja, L. L., "Fully coupled modeling of nanosecond pulsed plasma assisted combustion ignition," *Journal of Physics D: Applied Physics*, Vol. 52, No. 9, 2018, p. 095204.

- [10] Tholin, F., and Bourdon, A., "Simulation of the hydrodynamic expansion following a nanosecond pulsed spark discharge in air at atmospheric pressure," *Journal of Physics D: Applied Physics*, Vol. 46, No. 36, 2013, p. 365205.
- [11] Jasak, H., "OpenFOAM: open source CFD in research and industry," *International Journal of Naval Architecture and Ocean Engineering*, Vol. 1, No. 2, 2009, pp. 89–94.
- [12] Issa, R. I., "Solution of the implicitly discretised fluid flow equations by operator-splitting," *Journal of computational physics*, Vol. 62, No. 1, 1986, pp. 40–65.
- [13] Kurganov, A., and Tadmor, E., "New high-resolution central schemes for nonlinear conservation laws and convection-diffusion equations," *Journal of Computational Physics*, Vol. 160, No. 1, 2000, pp. 241–282.
- [14] Goodwin, D. G., Speth, R. L., Moffat, H. K., and Weber, B. W., "Cantera: An Object-oriented Software Toolkit for Chemical Kinetics, Thermodynamics, and Transport Processes," https://www.cantera.org, 2021. https://doi.org/10.5281/zenodo. 4527812, version 2.5.1.
- [15] Zhou, D., and Yang, S., "A robust reacting flow solver with detailed transport, chemistry, and steady-state preserving splitting schemes based on OpenFOAM and Cantera," AIAA Scitech 2020 Forum, 2020, p. 2139.
- [16] Zhou, D., Zou, S., and Yang, S., "An OpenFOAM-based fully compressible reacting flow solver with detailed transport and chemistry for high-speed combustion simulations," AIAA Scitech 2020 Forum, 2020, p. 0872.
- [17] Greenshields, C. J., Weller, H. G., Gasparini, L., and Reese, J. M., "Implementation of semi-discrete, non-staggered central schemes in a colocated, polyhedral, finite volume framework, for high-speed viscous flows," *International journal for numerical* methods in fluids, Vol. 63, No. 1, 2010, pp. 1–21.
- [18] Rusterholtz, D., Lacoste, D., Stancu, G., Pai, D., and Laux, C., "Ultrafast heating and oxygen dissociation in atmospheric pressure air by nanosecond repetitively pulsed discharges," *Journal of Physics D: Applied Physics*, Vol. 46, No. 46, 2013, p. 464010.
- [19] Castela, M., Stepanyan, S., Fiorina, B., Coussement, A., Gicquel, O., Darabiha, N., and Laux, C. O., "A 3-D DNS and experimental study of the effect of the recirculating flow pattern inside a reactive kernel produced by nanosecond plasma discharges in a methane-air mixture," *Proceedings of the Combustion Institute*, Vol. 36, No. 3, 2017, pp. 4095–4103.
- [20] Millikan, R. C., and White, D. R., "Systematics of vibrational relaxation," *The Journal of chemical physics*, Vol. 39, No. 12, 1963, pp. 3209–3213.
- [21] Rogallo, R. S., Numerical experiments in homogeneous turbulence, Vol. 81315, National Aeronautics and Space Administration, 1981.
- [22] Passot, T., and Pouquet, A., "Numerical simulation of compressible homogeneous flows in the turbulent regime," *Journal of Fluid Mechanics*, Vol. 181, 1987, pp. 441–466.
- [23] Cohen, S. D., Hindmarsh, A. C., and Dubois, P. F., "CVODE, a stiff/nonstiff ODE solver in C," Computers in physics, Vol. 10, No. 2, 1996, pp. 138–143.
- [24] Kurganov, A., Noelle, S., and Petrova, G., "Semidiscrete central-upwind schemes for hyperbolic conservation laws and Hamilton–Jacobi equations," SIAM Journal on Scientific Computing, Vol. 23, No. 3, 2001, pp. 707–740.
- [25] "PeleC Documentation," https://pelec.readthedocs.io/en/latest/, 2021.
- [26] Volpe, G., "Performance of compressible flow codes at low Mach numbers," AIAA journal, Vol. 31, No. 1, 1993, pp. 49-56.
- [27] Pletcher, R., and Chen, K.-H., "On solving the compressible Navier-Stokes equations for unsteady flows at very low Mach numbers," *11th Computational Fluid Dynamics Conference*, 1993, p. 3368.
- [28] Hsieh, S.-Y., and Yang, V., "A preconditioned flux-differencing scheme for chemically reacting flows at all Mach numbers," *International Journal of Computational Fluid Dynamics*, Vol. 8, No. 1, 1997, pp. 31–49.
- [29] Yang, S., Wang, X., Huo, H., Sun, W., and Yang, V., "An efficient finite-rate chemistry model for a preconditioned compressible flow solver and its comparison with the flamelet/progress-variable model," *Combustion and Flame*, Vol. 210, 2019, pp. 172–182.
- [30] Smith, G. P., Golden, D. M., Frenklach, M., Moriarty, N. W., Eiteneer, B., Goldenberg, M., Bowman, C. T., Hanson, R. K., Song, S., Gardiner Jr, W. C., et al., "GRI 3.0 Mechanism," *Gas Research Institute (http://www.me. berkeley. edu/gri_mech)*, 1999.